

Lattice Boltzmann method for thin-liquid-film hydrodynamics

S. Zitz,¹ A. Scagliarini,^{1,2,*} S. Maddu,^{1,3} A. A. Darhuber,⁴ and J. Harting^{1,4,†}

¹*Helmholtz Institute Erlangen-Nürnberg for Renewable Energy, Forschungszentrum Jülich, 90429 Nürnberg, Germany*

²*Institute for Applied Mathematics “M. Picone” (IAC), Consiglio Nazionale delle Ricerche, 00185 Rome, Italy*

³*Center for Systems Biology, Max Planck Institute of Molecular Cell Biology and Genetics, 01307 Dresden, Germany*

⁴*Department of Applied Physics, Eindhoven University of Technology, P. O. Box 513, 5600 MB Eindhoven, The Netherlands*



(Received 17 October 2018; revised manuscript received 7 June 2019; published 23 September 2019)

We propose an approach to the numerical simulation of thin-film flows based on the lattice Boltzmann method. We outline the basic features of the method, show in which limits the expected thin-film equations are recovered, and perform validation tests. The numerical scheme is applied to the viscous Rayleigh-Taylor instability of a thin film and to the spreading of a sessile drop toward its equilibrium contact angle configuration. We show that the Cox-Voinov law is satisfied and that the effect of a tunable slip length on the substrate is correctly captured. We address, then, the problem of a droplet sliding on an inclined plane, finding that the Capillary number scales linearly with the Bond number, in agreement with experimental results. At last, we demonstrate the ability of the method to handle heterogenous and complex systems by showcasing the controlled dewetting of a thin film on a chemically structured substrate.

DOI: [10.1103/PhysRevE.100.033313](https://doi.org/10.1103/PhysRevE.100.033313)

I. INTRODUCTION

Thin layers of liquids on solid surfaces are frequently encountered in a host of natural and technological settings [1,2]. Therefore, understanding and controlling their stability and dynamics is a central problem for fundamental physics, as well as for applied research in process engineering and nanotechnology [3,4]. Coating processes, for instance, rely crucially on the mutual affinity of liquid and surface (i.e., on wettability properties). When the liquid film is sufficiently thin, in fact, it can become unstable, leading to the dewetting of the coated area [5]. From the modeling point of view, the challenge consists in the fact that the physics of thin films is intrinsically multiscale, for it involves phenomena ranging from the molecular scale at the three-phase contact line to the micro- and nanometric size of the film thickness to the size of the film as a whole, extending over the coated substrate area.

A fully resolved bottom-up atomistic approach would be, obviously, unfeasible if hydrodynamic regimes are to be explored. It clearly appears that some degree of model order reduction is required. Most hydrodynamic models of thin liquid films, in the framework of the lubrication theory, simplify the complexity of the full three-dimensional (3D) Navier-Stokes equations [6,7] to one scalar transport equation (the lubrication equation) for the film thickness field $h(\mathbf{x}, t)$ [3,8–10]:

$$\partial_t h = \nabla \cdot [Q(h) \nabla p_{\text{film}}]. \quad (1)$$

Here $Q(h)$ is the mobility function, whose explicit form depends on the boundary condition for the velocity at the surface [for a no-slip boundary, $Q(h) = h^3/(3\mu)$, with μ being the dynamic viscosity], and p_{film} is the film pressure at the free liquid surface. Stable and reliable direct numerical

simulations of Eq. (1) require sophisticated numerical methods, whose execution is often computationally expensive [11]. Moreover, an ever-growing number of microfluidic problems requires us to cope with complex fluids rather than simple liquids, i.e., fluids with nontrivial internal microstructure and/or complex non-Newtonian rheological behavior (e.g., colloidal suspensions, polymer solutions, etc.). The quest for an efficient multiscale numerical method for simulating thin-film hydrodynamics, versatile for the inclusion of multiphysics features, is, thus, an ongoing endeavor.

In this paper, we present an approach to the numerical study of thin liquid films based on the lattice Boltzmann method (LBM) [12]. Due to the built-in properties of the LBM, our method enjoys an outstanding computational performance, especially on parallel architectures and graphics processing units (GPUs).

The paper is organized as follows. We first present the numerical model and discuss the equations of motion for the hydrodynamic fields that the model covers. We then show that these equations effectively correspond, under certain limits, to the lubrication equation of Reynolds. In Sec. III we present validation results, including the Rayleigh-Taylor instability of thin-fluid-films, the spreading of a sessile droplet on a substrate, and the sliding of a droplet on an inclined plane. After showcasing the ability of our method to handle large and heterogeneous substrates, we present some computational aspects including the performance of our implementation for GPUs. An Appendix is added to provide numerical tests of the validity of the correspondence with lubrication theory (Appendix).

II. NUMERICAL MODEL

When a layer of fluid is characterized by a vertical length scale H much smaller than the longitudinal one L , the

*andrea.scagliarini@cnr.it

†j.harting@fz-juelich.de

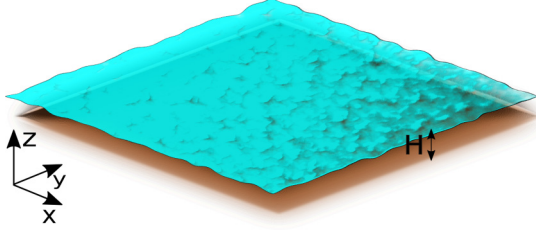


FIG. 1. Schematic sketch of a model system: a thin liquid film deposited on a flat substrate. The air-liquid interface is represented by the height $h(x, y, t)$. The characteristic thickness of the film is given by H .

equations of motion can be simplified under the approximation that the ratio of the length scales, $\varepsilon \equiv H/L$, is small ($\varepsilon \ll 1$, see Fig. 1). In this limit, and for small reduced Reynolds number, $\varepsilon^2 \text{Re}$ (where $\text{Re} = \frac{UL}{\nu}$, with U being a characteristic velocity of the fluid system and ν being the fluid's kinematic viscosity), the lubrication approximation tells that the dynamics is governed by Eq. (1). Instead of directly solving Eq. (1) numerically, we follow an alternative strategy. We build our numerical model on a class of LBMs originally proposed as solvers for the shallow-water equations [13–16]. The lattice Boltzmann equation for the discrete probability density functions of a fluid system subject to a total force (that can include both internal and external forces) \mathbf{F}_{tot} , $f_l(\mathbf{x}, t)$, reads:

$$f_l(\mathbf{x} + \mathbf{c}^{(l)} \Delta t, t + \Delta t) = (1 - \omega) f_l(\mathbf{x}, t) + \omega f_l^{(\text{eq})}(\mathbf{x}, t) + w_l \frac{\Delta t}{c_s^2} \mathbf{c}^{(l)} \cdot \mathbf{F}_{\text{tot}}, \quad (2)$$

where l labels the lattice velocities \mathbf{c}_l and runs from 0 to $Q - 1$, with Q being the number of velocities characterizing the scheme. Algorithmically, this equation can be seen as composed of two steps. There is a *local collision* step where the $f_l(\mathbf{x}, t)$ “relax” toward the local equilibrium distributions $f_l^{(\text{eq})}(\mathbf{x}, t)$ with rate $\omega = \Delta t / \tau$ (where τ , the relaxation time, is proportional to the kinematic viscosity ν): The distribution functions are substituted by their weighted average (with weights ω and $1 - \omega$) with the equilibria, with an added “source” term [the last term on the right-hand side of Eq. (2)], when a force is present. There is a *nonlocal streaming* step where the updated distribution functions are scattered to the nearest-neighboring sites. The parameters c_s (the lattice speed of sound) and w_l (the “weights”) depend on the geometry of the lattice and are determined under suitable constraints on the form of the tensorial moments in the lattice velocities up to fourth order [17]. We work with two-dimensional square lattices of side length $N\Delta x$, with lattice constant Δx and $Q = 9$. For simplicity, we keep $\Delta t = \Delta x = 1$ throughout this paper and follow the standard notation, where $c_s = 1/\sqrt{3}$ and the $\mathbf{c}^{(l)} = [c_x^{(l)}, c_y^{(l)}]$, $l = 0, 1, \dots, 8$, are [18,19]

$$\mathbf{c}^{(l)} = \begin{cases} (0, 0) & l = 0 \\ [\cos \frac{(l-1)\pi}{4}, \sin \frac{(l-1)\pi}{4}] & l = 1, 3, 5, 7, \\ \sqrt{2} [\cos \frac{(l-1)\pi}{4}, \sin \frac{(l-1)\pi}{4}] & l = 2, 4, 6, 8 \end{cases} \quad (3)$$

with the corresponding weights

$$w_l = \begin{cases} \frac{4}{9} & l = 0 \\ \frac{1}{9} & l = 1, 3, 5, 7. \\ \frac{1}{36} & l = 2, 4, 6, 8 \end{cases} \quad (4)$$

The equilibrium distribution functions $f_l^{(\text{eq})}$ have to be determined to recover the desired equations of motion for hydrodynamic fields in the long-wavelength limit (we will return to this shortly). They have, therefore, to fulfill the following relations involving the liquid height

$$h = \sum_{l=0}^8 f_l^{(\text{eq})}, \quad (5)$$

momentum

$$hu_i = \sum_{l=0}^8 c_i^{(l)} f_l^{(\text{eq})}, \quad (6)$$

and momentum flux tensor field

$$\frac{1}{2} gh^2 \delta_{ij} + hu_i u_j = \sum_{l=0}^8 c_i^{(l)} c_j^{(l)} f_l^{(\text{eq})}, \quad (7)$$

where the left-hand side coincides with the momentum flux of the shallow-water equation, with the term $gh^2/2$ being the hydrostatic pressure in a thin fluid layer at rest [14]. With the usual *ansatz* of a quadratic polynomial in the velocity field \mathbf{u} , the equilibrium distribution functions read

$$f_l^{(\text{eq})} = \begin{cases} h - \frac{5gh^2}{6c_s^2} - \frac{2hu^2}{3c_s^2} & l = 0 \\ \frac{gh^2}{6c_s^2} + \frac{hc^{(l)} \cdot \mathbf{u}}{3c_s^2} + \frac{h[\mathbf{c}^{(l)} \cdot \mathbf{u}]^2}{2c_s^4} - \frac{hu^2}{6c_s^2} & l = 1, 3, 5, 7, \\ \frac{gh^2}{24c_s^2} + \frac{hc^{(l)} \cdot \mathbf{u}}{12c_s^2} + \frac{h[\mathbf{c}^{(l)} \cdot \mathbf{u}]^2}{8c_s^4} - \frac{hu^2}{24c_s^2} & l = 2, 4, 6, 8 \end{cases} \quad (8)$$

where $u^2 = |\mathbf{u}|^2$ is the magnitude of the velocity. The multi-scale Chapman-Enskog expansion [20,21] of such an LBM yields (for small ratios Ma/Fr of the Mach, $\text{Ma} = u/c_s$, and Froude, $\text{Fr} = u/\sqrt{gH}$, numbers, corresponding also to $\sqrt{gH}/c_s \ll 1$) the following equations for the height and velocity fields [13,14,16]:

$$\begin{cases} \partial_t h + \nabla \cdot (h\mathbf{u}) = 0 \\ \partial_t (h\mathbf{u}) + \nabla \cdot (h\mathbf{u}\mathbf{u}) = -gh\nabla h \\ + \nu \nabla^2 (h\mathbf{u}) + 2\nu \nabla \cdot (\nabla \cdot (h\mathbf{u})) + \mathbf{F}_{\text{tot}} \end{cases}, \quad (9)$$

where ν , the kinematic viscosity, is related to the relaxation rate ω appearing in (2) via $\nu = c_s^2 [(2 - \omega)/2\omega] \Delta t$. For stability of the scheme, the condition $\text{Fr} < 1$ is also required, which is fulfilled in all our applications, given the low values of u (as discussed in more detail later). Different terms contribute to the total (generalized) force \mathbf{F}_{tot} :

$$\mathbf{F}_{\text{tot}} = \mathbf{F}_{\text{film}} + \mathbf{F}_{\text{fric}} + \mathbf{F}. \quad (10)$$

¹The generalized forces have indeed the dimensions of $(\text{length})^2(\text{time})^{-2}$.

In the first term the film pressure appearing in (1) is included as $\mathbf{F}_{\text{film}} = -\frac{1}{\rho_0}h\nabla p_{\text{film}}$, where the film pressure p_{film} is written as

$$p_{\text{film}} = -\gamma[\nabla^2 h - \Pi(h)] \quad (11)$$

and ρ_0 is the (constant) liquid density (equal to 1 in LBM units). The first term in Eq. (11) represents the capillary Laplace pressure (with γ being the surface tension) while the second term is the disjoining pressure. Various forms have been proposed for $\Pi(h)$ in the literature [3,22], where here we use the expression

$$\begin{aligned} \Pi(h) = \kappa f(h) = & \underbrace{[1 - \cos(\theta)]}_{\kappa} \frac{(n-1)(m-1)}{(n-m)h_*} \\ & \times \underbrace{\left[\left(\frac{h_*}{h}\right)^n - \left(\frac{h_*}{h}\right)^m \right]}_{f(h)}. \end{aligned} \quad (12)$$

In Eq. (12), θ is the contact angle and h_* corresponds to the precursor film thickness. The integers n and m are set to be 3 and 9, respectively. These are commonly chosen values in the literature [3,23] that correspond to a standard 6-12 Lennard-Jones intermolecular potential [24], though other pairs (n, m) can be used [e.g., (2, 3), (3, 6), (4, 10)] [25–27]. By adjusting κ we are thus able to address the wetting properties of the substrate. The film pressure is specific to model thin-film dynamics; in general, however, one can make use of other force terms, e.g., to couple fluid layers which has been shown in Ref. [28]. The second term on the right-hand side in Eq. (10) introduces a friction with the substrate of the form

$$\mathbf{F}_{\text{fric}} = -\nu\alpha_\delta(h)\mathbf{u} \quad (13)$$

with the coefficient $\alpha_\delta(h)$ given by

$$\alpha_\delta(h) = \frac{6h}{(2h^2 + 6\delta h + 3\delta^2)}. \quad (14)$$

Here δ acts as a regularizing parameter, which can be identified with an effective slip length. Finally, the last term in Eq. (10), \mathbf{F} , accounts for any other possible source of forcing (e.g., the gravity component parallel to the substrate in the case of a liquid-film deposited on an inclined plate). Equipped with such extra terms, Eqs. (9) become

$$\begin{cases} \partial_t h + \nabla \cdot (h\mathbf{u}) = 0 \\ \partial_t (h\mathbf{u}) + \nabla \cdot (h\mathbf{u}\mathbf{u}) = -gh\nabla h \\ + \nu\nabla^2 (h\mathbf{u}) + 2\nu\nabla[\nabla \cdot (h\mathbf{u})] - \frac{1}{\rho_0}h\nabla p_{\text{film}} - \nu\alpha_\delta(h)\mathbf{u} + \mathbf{F}. \end{cases} \quad (15)$$

Let us notice at this point that for most microfluidic applications we are actually interested in, the advection term on the left-hand side of the second equation of (15) is indeed negligible as compared to the right-hand side (the Reynolds number [29,30] being much smaller than one). Analogously, the longitudinal viscous terms $\nu\nabla^2 (h\mathbf{u})$ and $2\nu\nabla[\nabla \cdot (h\mathbf{u})]$ are of order ε^2 smaller in the ratio of length scales than the friction term $\nu\alpha(h)\mathbf{u}$ (since the former scale as $\nu H \frac{U}{L^2}$, whereas the latter as $\nu \frac{U}{H}$). Therefore they can also be neglected. The validity of these considerations has been numerically tested in some selected cases (representative of

typical applications) and the results are shown and discussed in the Appendix. Equations (15) reduce then to

$$\begin{cases} \partial_t h + \nabla \cdot (h\mathbf{u}) = 0 \\ \partial_t (h\mathbf{u}) = -gh\nabla h - \frac{1}{\rho_0}h\nabla p_{\text{film}} - \nu\alpha_\delta(h)\mathbf{u} + \mathbf{F}. \end{cases} \quad (16)$$

For processes evolving on timescales \tilde{t} such that $\tilde{t} \gg \frac{h}{\alpha(h)\nu}$, one can consider the “quasisteady” limit of the second of these equations [setting $\partial_t (h\mathbf{u}) \approx 0$], which yields

$$\mathbf{u} \approx \frac{1}{\nu\alpha_\delta(h)} \left(-gh\nabla h - \frac{1}{\rho_0}h\nabla p_{\text{film}} + \mathbf{F} \right), \quad (17)$$

effectively enslaving the dynamics of \mathbf{u} to that of h . In the no-slip limit, $\delta \rightarrow 0$, and in absence of gravity and other forces, Eq. (17) simplifies into

$$\mathbf{u} \approx -\frac{h^2}{3\mu} \nabla p_{\text{film}}$$

with the dynamic viscosity $\mu = \rho_0\nu$. Inserting this result into the first equation of (16) leads to

$$\partial_t h \approx \nabla \cdot \left(\frac{h^3}{3\mu} \nabla p_{\text{film}} \right),$$

which is precisely the lubrication equation. In essence, our method is, therefore, an alternative solver of the lubrication equation (at least in the inertialess regime, $\text{Re} \ll 1$, and for very thin films, $\varepsilon \ll 1$), that brings in, from the computational point of view, the added values of excellent scalability of the corresponding LBM algorithm on parallel architectures, as we shall see in the following sections. Similar ideas have also been developed for reaction-diffusion equations [31–34] and the modeling of surface tension effects by gradients of auxiliary fields [35,36] based on the color gradient method [37].

Before concluding this section, let us notice that special care has to be taken in the implementation of the numerical scheme, when evaluating the forcing term since it contains higher-order derivatives [the gradient p_{film} , which in turn includes the Laplace pressure $\gamma\nabla^2 h$, see Eq. (11)] and, hence, spurious lattice effects may arise. We noticed, for example, that a centered scheme to calculate gradients [15] does not guarantee the sufficient degree of isotropy on the lattice as, e.g., for the relaxation of a droplet (discussed in Sec. III), where it led to unphysical droplet shapes. Therefore, we use the following expressions to compute the gradients:

$$\nabla\phi(\mathbf{x}) = 3 \sum_{l=0}^8 w_l \mathbf{c}^{(l)} \phi(\mathbf{x} + \mathbf{c}^{(l)}) + O(\nabla^3), \quad (18)$$

and the Laplacian

$$\begin{aligned} \nabla^2\phi(\mathbf{x}) = & \frac{1}{6} \left[4 \sum_{l=\text{odd}} w_l \phi(\mathbf{x} + \mathbf{c}^{(l)}) \right. \\ & \left. + 1 \sum_{l=\text{even}} w_l \phi(\mathbf{x} + \mathbf{c}^{(l)}) - 20\phi(\mathbf{x}) \right] + O(\nabla^4), \end{aligned} \quad (19)$$

respectively [38,39], for a generic scalar field ϕ (be it the height field h , the pressure p_{film} , or a position-dependent surface tension field). Besides the higher degree of the isotropy,

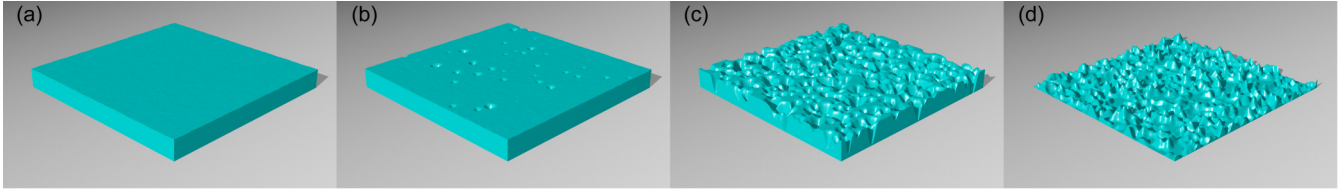


FIG. 2. Time evolution of the free surface for the Rayleigh-Taylor instability at $\tau_{\text{cap}} \approx 50, 75, 100, 188$, corresponding to the lattice Boltzmann time steps [9000, 14000, 19000, 35000] Δt in (a)–(d). For a more clear visualization we only show a small patch of size 256×256 centered in the middle of the 2048×2048 domain. The fluctuations of earlier states still follow the linear stability analysis (see Fig. 3 for the the power spectrum of the height fluctuations versus wave number).

the scheme (18) and (19) has the advantage of employing directly the set of lattice Boltzmann speeds.

III. RESULTS

Below we present results from numerical simulations using the method introduced in the previous section. For all simulations, we apply periodic boundary conditions in the X - Y plane.

A. The Rayleigh-Taylor instability

The Rayleigh-Taylor instability occurs when a denser fluid is accelerated against a less dense one [40–43]. This can be the case, for instance, for a liquid film coating a ceiling under the action of gravity. In such a configuration gravity tends, of course, to deform (and eventually disrupt) the film, while surface tension has a stabilizing effect. As a result of these competing mechanisms, any surface perturbation is stable or unstable depending on whether its characteristic wave number k is smaller or larger than a certain critical value k_c . Linear stability analysis calculations in the framework of lubrication theory provide the following growth rate $\sigma(k)$:

$$\sigma(k) = \frac{\rho g h_0^3}{3\mu} (k^2 - l_{\text{cap}}^2 k^4), \quad (20)$$

where $l_{\text{cap}} = (\gamma/g)^{1/2}$ is the capillary length. Unstable (stable) modes correspond to $\sigma(k) > 0$ [$\sigma(k) < 0$] and the critical wave number is, therefore, such that $\sigma(k_c) = 0$, i.e., $k_c = 1/l_{\text{cap}}$. On a lattice of size 2048×2048 nodes, we initialize the film height according to

$$h(\mathbf{x}, 0) = h_0[1 + \varepsilon(\mathbf{x})], \quad (21)$$

with ε a random variable homogeneously distributed in $[1 \times 10^{-4}, -1 \times 10^{-4}]$ and $h_0 = 1$. Forcing should always be below a certain threshold. Thus, for the gravitational acceleration we choose values within the interval $|g| = [4, 8] \times 10^{-5}$. Furthermore, we fix the surface tension to be $\gamma = 0.01$. This results in critical wave numbers ranging from $k_c = 0.06$ to $k_c = 0.09$. Figure 2 shows snapshots of the free surface from various time steps, where the growth of the perturbations is shown as time increases. The last panel is already beyond the linear regime.

We consider the time evolution of the power spectrum of the height field fluctuations (around the mean), defined as

$$E(k, t) = \oint_{\Omega_k} |\delta h(\mathbf{k}, t)|^2 d\Omega_k, \quad (22)$$

where

$$\delta h(\mathbf{k}, t) = \int e^{-2\pi i \mathbf{k} \cdot \mathbf{x}} [h(\mathbf{x}, t) - h_0] d\mathbf{x}, \quad (23)$$

with $\mathbf{k} = (k_x, k_y)$. Ω_k denotes the circle in \mathbf{k} space (i.e., $\Omega_k = \{(k_x, k_y) | k_x^2 + k_y^2 = k^2\}$). Since we work in a discretized system we have to smear out the circle Ω_k with some small δk . Therefore, strictly speaking the integral is not computed around the circle Ω_k but around some small annulus $\Omega_{k+\delta k}$. The spectra are shown in Fig. 3. The various colors and symbols of Fig. 3 relate to different values of gravitational acceleration. For every set we consider the spectra at three equally scaled times $\tilde{t} = t/\tau_{\text{cap}}$, where

$$\tau_{\text{cap}} = \frac{\mu l_c}{\gamma}, \quad (24)$$

$\tilde{t} = 50, 75, 100$. The values of k_c correspond to the points where the colored lines with symbols cut the black dashed line. The horizontal colored dashed lines mark the theoretical values for k_c . We observe good agreement of theoretical and numerical values. In the inset of Fig. 3 we plot the growth rate for the data of $g = 8 \times 10^{-5}$ together with the theoretical expression given by Eq. (20) (solid line).

Consistently with the random initialization, at $\tilde{t} = 0$ the spectrum is a constant (black dashed line). For $\tilde{t} > 0$, $E(k, t)$

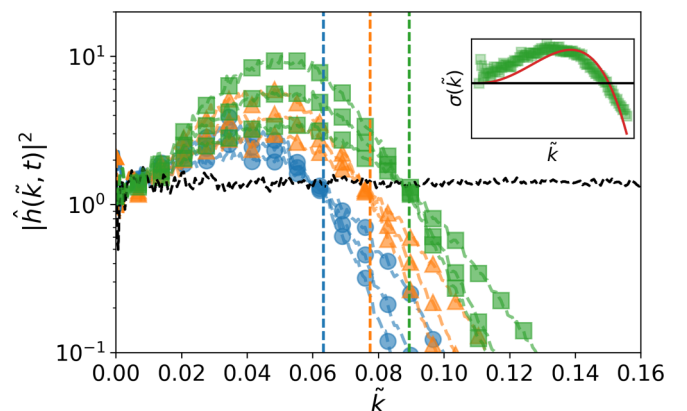


FIG. 3. Power spectrum of the height fluctuations versus wave number. The different colors and symbols belong to different values of gravitational acceleration; $g = 4 \times 10^{-5}$ is given by blue circles (\bullet), $g = 6 \times 10^{-5}$ by orange triangles (\blacktriangle), and $g = 8 \times 10^{-5}$ is given by green squares (\blacksquare). Same colored lines are taken at different time steps. In the inset we show the growth rate $\sigma(k)$ for the largest value of g (symbols) and the theoretical growth rate according to Eq. (20) (solid line).

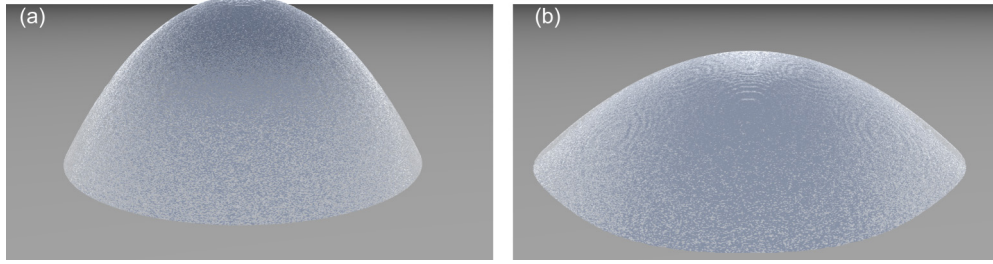


FIG. 4. Relaxation of an out-of-equilibrium droplet. The initial state (a) is shown with a contact angle of $\theta = \pi/6$. Toward the end of the simulation (b) the droplet relaxes to the equilibrium contact angle.

develops a profile that grows in time for $k < k_c$, while it is damped out for $k > k_c$, in agreement with the expectation from the theory.

B. A spreading droplet

Let us consider the problem of a droplet, deposited on a smooth substrate with an apparent contact angle $\theta > \theta_{eq}$, which spreads to relax to a shape dictated by the equilibrium contact angle θ_{eq} . The equilibrium contact angle quantifies the wettability of a given substrate by a certain liquid and can be calculated using Young's equation [44],

$$\gamma \cos \theta_{eq} = \gamma_{SL} - \gamma_{SG}, \quad (25)$$

with γ_{SL} and γ_{SG} being the surface tensions between solid-liquid and solid-gas, respectively.

In our simulations we set the equilibrium contact angle through the disjoining pressure [Eq. (12)]. In order to comply as much as possible with the thin-film assumptions, we limit ourselves to relatively small contact angles.

To probe the spreading, on a 512×512 lattice we initialize a droplet whose surface is given by the expression

$$h(x, y, 0) = \sqrt{R^2 - (x - x_0)^2 - (y - y_0)^2} - R \cos \theta, \quad (26)$$

with $R \sin \theta \approx 100\Delta x$ ($\theta > \theta_{eq}$) being the radius of the droplet with a spherical cap shape and (x_0, y_0) its center. The droplet is placed in the center of the lattice, i.e., $x_0 = y_0 = 256\Delta x$.

In Fig. 4 we show such an initial shape, with contact angle $\theta = \pi/6$, and the equilibrium shape with contact angle $\theta_{eq} = \pi/12$.

To extract the contact angle from our data we impose that the shape at all times is close to the shape of a spherical cap, such that we are able to calculate the contact angle at any time using the initial angle and radius to obtain the volume

$$V = \frac{\pi}{3} R^3 (2 + \cos \theta) (1 - \cos \theta)^2. \quad (27)$$

Since our method is mass conserving, the volume of the droplet is by construction conserved. Measuring both the height of the droplet $h_d(t)$ and the diameter of the spherical cap $2r(t)$ we are able to recalculate the time-dependent sphere radius as

$$R(t) = \frac{r(t)^2 + h_d(t)^2}{2h_d(t)} \quad (28)$$

and can solve Eq. (27) again for the contact angle $\theta(t)$. We cross-checked our results with an alternative approach to

calculate the angle given by

$$\theta(t) = \sin \left[\frac{r(t)}{R(t)} \right]^{-1}. \quad (29)$$

Let us stress that the shape is indeed very close to a spherical cap. As mentioned in Sec. II, in fact, a sufficiently accurate finite-difference scheme is required, as the one in Eqs. (18)–(19) [39]. In particular, we note that the isotropy of the pressure gradient is of utmost importance: A simple scheme with two-point centered derivatives [15] yields squared equilibrium droplet shapes.

The spreading dynamics can be investigated even more quantitatively in terms of the so-called Cox-Voinov law and Tanner's law [45]. The first one relates the apparent contact angle to the velocity U of the spreading front (the contact line), at various times, by $\theta^3 - \theta_{eq}^3 \propto Ca$. The capillary number Ca is defined as $Ca = \mu U / \gamma$ [46]. In Fig. 5 we plot $\theta^3(t) - \theta_{eq}^3$ vs. $Ca(t)$ from a numerical simulation of a spreading drop: A good linear scaling, in agreement with the Cox-Voinov law, is observed, as highlighted by the dashed line. Tanner's law states that the radius of the droplet grows with time as

$$R(t) \approx \left[\frac{10\gamma}{9B\mu} \left(\frac{4V}{\pi} \right)^3 t \right]^{1/10}, \quad (30)$$

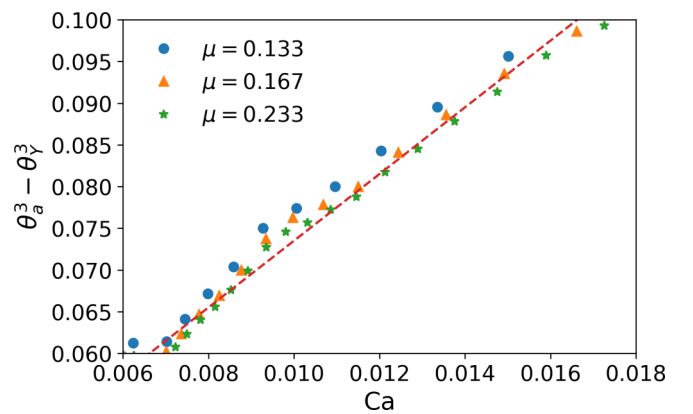


FIG. 5. Difference of cubed instantaneous and equilibrium contact angles, $\theta_{num}^3 - \theta_{eq}^3$, vs. capillary number Ca for a spreading droplet; the dashed line shows a linear dependence (consistent with the Cox-Voinov law). The different symbols represent different viscosities, while the dashed line is a linear function of the capillary number.

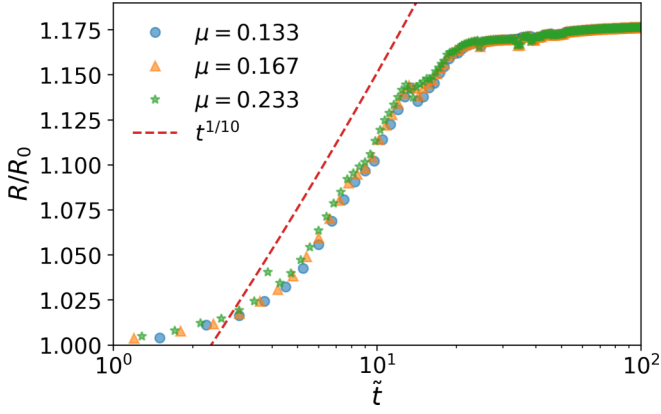


FIG. 6. Time evolution of the droplet base radius of a spreading droplet; the dashed red line shows a $\tilde{t}^{1/10}$ power law (consistent with Tanner's law). As in Fig. 5 different symbols refer to different viscosities. The radius clearly grows with the predicted power law until it saturates. On rescaling the time with τ_{cap} the curves of all three viscosities collapse into a single one.

with the constant B being such that $B^{1/10} \approx 1.2$. In Fig. 6 we plot the measured radius of the droplet divided by its initial radius R_0 as a function of the dimensionless time $\tilde{t} = t/\tau_{\text{cap}}$ (here $\tau_{\text{cap}} = \frac{\mu R}{\gamma}$). For the three viscosities considered in Figs. 5 and 6 our capillary times are $\tau_{\text{cap}} = [1333, 1667, 2333]\Delta t$. We see a saturation at $R/R_0 = 1.17$ because the droplet is very close to its equilibrium shape. During the growth phase the radius follows indeed a power law in \tilde{t} with exponent $1/10$, which is shown by the red dashed line, in agreement with Tanner's prediction and experimental results [47–50]. We further notice that within our simulations the droplet needs about $12\tau_{\text{cap}}$ to reach its equilibrium shape.

C. A Sliding droplet

As a further validation case we consider the sliding of a droplet on an inclined plane. For a droplet to slide over an inclined plane, a minimum tilting angle $\alpha > 0$ of the substrate is required [51], which in our case is due to the friction term Eq. (14). Until this critical angle is reached, energy is stored in the deformation of the surface as the upper-left inset in Fig. 7 shows. Above such a critical angle, a linear relation between the terminal sliding velocity U_∞ and the gravitational force $\propto mg \sin \alpha$ is observed [52–54]; in dimensionless numbers such behavior is expressed by

$$\text{Ca} \propto \text{Bo} - \text{Bo}_c, \quad (31)$$

where the capillary number is based on U_∞ and Bo is the so-called Bond number, given by

$$\text{Bo} = (3V/4\pi)^{2/3} \rho g \frac{\sin \alpha}{\gamma}. \quad (32)$$

Bo_c is the critical Bond number, defined in terms of the critical tilting angle α_c . In Fig. 7 we plot Ca vs. Bo from our numerical simulations, showing that the phenomenology described by Eq. (31) is indeed reproduced, i.e., the onset of sliding takes place at a finite forcing, beyond which the linear scaling $\text{Ca} \sim \text{Bo}$ is fulfilled.

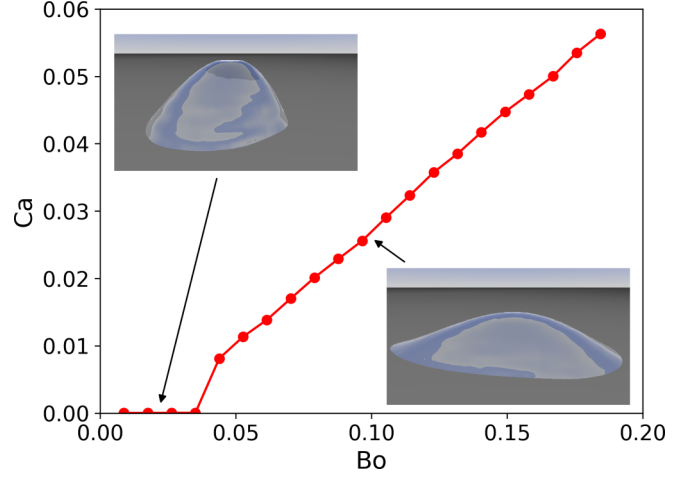


FIG. 7. Ca vs. Bo for a sliding droplet: Notice that a finite minimum forcing (corresponding to Bo_c) is needed to actuate the droplet. For $\text{Bo} > \text{Bo}_c$ a linear relation, $\text{Ca} \sim \text{Bo}$, is observed. In the insets we show the shape of the droplet for both the pinned (upper left) as well as the sliding (lower right) case.

D. Dewetting of liquid films

In order to showcase the capabilities of our method in handling more complex physics scenarios, we finally consider the dewetting of a chemically patterned substrate [55,56]. This is easily made possible within the code by introducing a space-varying equilibrium contact angle, $\theta_{\text{eq}}(x, y)$, in Eq. (12); in this way we can tune the local wettability of the substrate. Figure 8 shows a liquid film which is initialized with thickness $h(x, y, 0)$ randomly fluctuating in space around its mean value h_0 by a small percentage ($\approx 0.01\%$) of it [Fig. 8(a)]. A partially wettable substrate is patterned in such a way that the contact angle is lower on a region defining a logo. The total domain contains 512×512 lattice nodes. With this domain size a letter contains around 130 lattice nodes in the y direction and about 60 lattice nodes in the x direction. Using the initial height h_0 of the film as characteristic length scale we get a capillary time of $\tau_{\text{cap}} \approx 20\Delta t$. As the film dewets, liquid moves toward the letters of the logo, the surrounding film becomes thinner, and eventually the logo becomes visible.

IV. COMPUTATIONAL ASPECTS

We use OpenACC directives to allow our code to run on accelerator devices, such as GPUs, while being able, at the same time, to exploit the well-known good scaling properties of the LBM on parallel machines [57]. OpenACC is particularly versatile in terms of programmability since it only requires a few lines of code to allow us to harness the power of state-of-the-art accelerators. In this sense OpenACC is very similar to OpenMP and more readable as well as much easier to program than CUDA.

The performance of a LBM code is commonly measured in million lattice updates per second (MLUPS), defined as

$$\text{MLUPS} = \frac{A \times n}{t_{\text{sim}} \times 10^6}, \quad (33)$$

with $A = L_x \times L_y$ being the area of the lattice, where L_x, L_y are the number of lattice nodes in the x and y directions.



FIG. 8. Time evolution of the free surface on a chemically patterned substrate on a $512 \times 512 \Delta x^2$ domain. Varying the contact angle between the letters and the rest of the substrate yields the shown dewetting pattern. The letters are more wettable than the rest. To emphasize the process we use a color gradient ranging from dark blue to light blue. Starting from a randomly perturbed film height, the fluid starts to dewet the pattern and after $2400\Delta t$ the letters and a surrounding rim structure are clearly visible (a). After $16800\Delta t$ a depletion around the letters is already very prominent (b). Toward the end of the simulation at $97200\Delta t$, the instability of the thin film also leads to film rupture. Holes form among the letters E, R, and N (c).

The number of iterations is given by n . The time needed to compute the n iterations is called t_{sim} (in seconds). In Table I we provide benchmark data comparing the performance of a Nvidia GTX 1080TI, a Nvidia Quadro K2200, and a single core of an Intel i7-4790 @ 3.6-GHz CPU. Due to the limited amount of memory available on the Quadro K2200, it is not possible to run a simulation of size 4096^2 on this card. Such a simulation requires about 4.8 GB local memory, while the Quadro K2200 only supplies 4 GB. In particular the speedup gained by using a GTX 1080TI is outstanding and corresponds to about 24–92 times the performance of a single core of the Intel CPU. Assuming perfect scaling on the CPU and using all four physical cores, the simulation on the GPU would be faster by a factor between 6 and 23. The speedup depends on the size of the lattice and in order to keep the pipelines on the GPU filled, a minimum loop size is needed. In addition, data transfer between *host* and *device* is a known bottleneck impacting the performance of GPU-based simulations. This is obviously also the case for our code—even though such data transfer is only needed when files are written to disk.

V. CONCLUSIONS

We have presented a lattice Boltzmann model for the numerical simulation of thin liquid-film hydrodynamics, featuring explicitly relevant properties of interface physics, such as surface tension and disjoining pressure.

We validated our method against a relevant test case, namely the Rayleigh-Taylor instability, where the critical wave number as well as the growth and damping of wave modes are correctly reproduced. Our simulations of droplets on substrates showed that droplets initiated out of equilibrium attain their equilibrium contact angle and that our method correctly reproduces the Cox-Voinov law as well as Tanner’s law.

TABLE I. Performance analysis based on a MLUPS measurement. The different columns relate to different lattice sizes, while the rows correspond to the two GPUs and one CPU used. All simulations are run for $100000\Delta t$ with FP64 double precision.

Lattice/accelerator	128^2	256^2	512^2	1024^2	2048^2	4096^2
GTX 1080TI	157.6	279.2	382.6	414.9	404.7	395.6
Quadro K2200	33.5	42.9	46.6	48.2	49.0	X
i7-4790	6.4	5.8	4.5	4.6	4.5	4.3

Furthermore, our approach allows us to simulate the dynamics of sliding droplets and even complex dewetting scenarios.

Our OpenACC-enabled simulation code allows for a massive improvement of the performance: With modern GPU cards at hand simulations using large lattice sizes and requiring many time steps can be run on a single workstation without the need for access to high-performance computing resources.

In the future, we plan to extend our work toward systems which could hardly be tackled by traditional methods: From the dynamics of individual droplets on complex shaped substrates we plan to move to large numbers of droplets in order to understand the statistical properties of collective droplet motion on chemically structured substrates. Finally, a possible application of our method could be the simulation of full laboratory-on-chip devices with highly resolved channels, junctions, and so on.

ACKNOWLEDGMENTS

The authors acknowledge financial support by the Deutsche Forschungsgemeinschaft (DFG) within the Cluster of Excellence “Engineering of Advanced Materials” (Project No. EXC 315) (Bridge Funding). The work has been partly performed under the Project HPC-EUROPA3 (INFRAIA-2016-1-730897), with the support of the EC Research Innovation Action under the H2020 Programme; in particular, S.Z. gratefully acknowledges the support of Consiglio Nazionale delle Ricerche (CNR) and the computer resources and technical support provided by CINECA.

APPENDIX

As anticipated above, we provide here a numerical validation of the assumptions on effectively negligible terms that lead from Eq. (9) to Eq. (16). To this aim, we report in Fig. 9, for each of the term under scrutiny, the time evolution of a L_2 norm, defined for a generic scalar field $\phi(\mathbf{x}, t)$ as

$$\|\phi(t)\|_2 = \left\{ \frac{1}{N^2} \sum_{i=1}^N \sum_{j=1}^N [\phi(x_i, y_j, t)]^2 \right\}^{\frac{1}{2}}, \quad (\text{A1})$$

where the double sum is extended to the whole two-dimensional domain. Three case studies are analyzed (corresponding to the three panels in Fig. 9), namely (a) a sessile droplet spreading on a substrate with an equilibrium

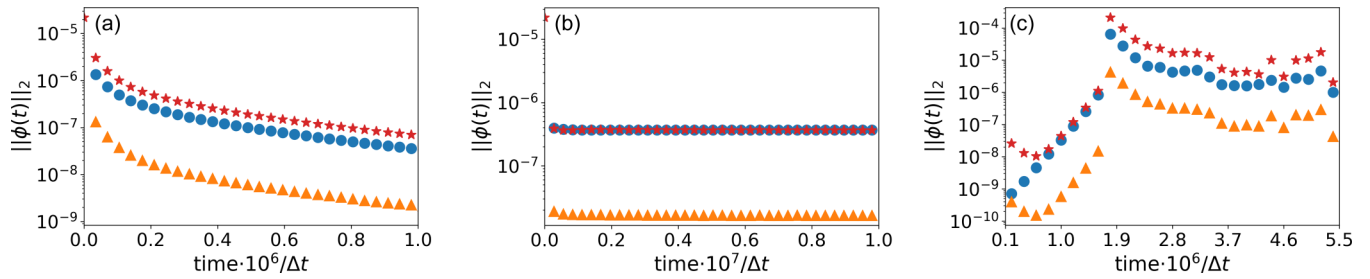


FIG. 9. Time evolution of the L_2 norm [as defined by Eq. (A1)] of the x component of the terms appearing on the right-hand side of the second of Eqs. (15). The plot is in log-linear scale. The panels refer to three different numerical experiments: (a) spreading droplet, (b) sliding droplet, and (c) thin-film dewetting. The symbols correspond to film pressure gradient, $-\partial_x p_{\text{film}}$ (\star); friction, $-\nu\alpha(h)u_x$ (\bullet); and longitudinal dissipation terms $\nu\nabla^2(hu_x) + 2\nu\partial_x[\nabla \cdot (hu)]$, (\blacktriangle).

contact angle smaller than the initial one, (b) a droplet sliding under the action of a body force, and (c) the dewetting of a substrate. We compare, for each simulation, the $\|\phi(t)\|_2$ for the x component² of the gradient of the film pressure, $-\partial_x p_{\text{film}}$, of the friction term, $-\nu\alpha(h)u_x$, and of the lon-

gitudinal viscous terms, $\nu\nabla^2(hu_x) + 2\nu\partial_x[\nabla \cdot (hu)]$ [the advection term, $\nabla \cdot (huu_x)$ is for all cases orders of magnitude smaller than the other terms, therefore we decided to omit it from the comparisons in figure Fig. 9]. We observe that the gradient of the film pressure and the friction are dominant, with the L_2 norm of the longitudinal dissipation term being always, roughly, less than 10% of the friction contribution.

²Similar results are found also for the y component.

- [1] P. de Gennes, F. Brochard-Wyart, and D. Quere, *Capillarity and Wetting Phenomena: Drops, Bubbles, Pearls, Waves* (Springer, New York, 2003).
- [2] M. Focke, D. Kosse, C. Müller, H. Reinecke, and F. von Stetten, *Lab Chip* **10**, 1365 (2010).
- [3] A. Oron, S. H. Davis, and S. G. Bankoff, *Rev. Mod. Phys.* **69**, 931 (1997).
- [4] A. S. Utada, L.-Y. Chu, A. Fernández-Nieves, D. R. Link, C. Holtze, and D. A. Weitz, *MRS Bull.* **32**, 702 (2007).
- [5] D. Bonn, J. Eggers, J. Indekeu, J. Meunier, and E. Rolley, *Rev. Mod. Phys.* **81**, 739 (2009).
- [6] C. L. Navier, *Mém. l'Acad. sci. l'Inst. France* **6**, 389 (1823).
- [7] G. G. Stokes, *Trans. Cambridge Philos. Soc.* **7**, 439 (1842).
- [8] O. Reynolds, *Philos. Trans. R. Soc. Lond.* **177**, 157 (1886).
- [9] R. V. Craster and O. K. Matar, *Rev. Mod. Phys.* **81**, 1131 (2009).
- [10] V. Mitlin, *J. Colloid Interface Sci.* **156**, 491 (1993).
- [11] J. Becker, G. Grün, R. Seemann, H. Mantz, K. Jacobs, K. R. Mecke, and R. Blossey, *Nat. Mater.* **2**, 59 (2003).
- [12] S. Succi, *The Lattice Boltzmann Equation for Fluid Dynamics and Beyond* (Oxford Science, Oxford, 2001).
- [13] R. Salmon, *J. Mar. Res.* **57**, 503 (1999).
- [14] P. J. Dellar, *Phys. Rev. E* **65**, 036309 (2002).
- [15] J. G. Zhou, *Lattice Boltzmann Methods for Shallow Water Flows*, Vol. 4 (Springer, Berlin, 2004).
- [16] P. Van Thang, B. Chopard, L. Lefèvre, D. A. Ondo, and E. Mendes, *J. Comput. Phys.* **229**, 7373 (2010).
- [17] D. A. Wolf-Gladrow, *Lattice-Gas Cellular Automata and Lattice Boltzmann Models: An Introduction* (Springer, Berlin, 2001).
- [18] Y. H. Qian, D. d'Humières, and P. Lallemand, *Europhys. Lett.* **17**, 479 (1992).
- [19] X. Shan, X. F. Yuan, and H. Chen, *J. Fluid. Mech.* **550**, 413 (2006).
- [20] S. Chapman and T. G. Cowling, *The Mathematical Theory of Non-uniform Gases* (Cambridge University Press, Cambridge, 1939).
- [21] D. Enskog, *Kinetische Theorie der Vorgänge in mässig verdünnten Gasen*, Ph.D. thesis, 1917.
- [22] U. Thiele, *Adv. Colloid Interface Sci.* **206**, 399 (2014).
- [23] D. E. Moulton and J. Lega, *Eur. J. Appl. Math.* **24**, 887 (2013).
- [24] J. Fischer and G. Grün, *SIAM J. Math. Anal.* **50**, 411 (2018).
- [25] J. A. Diez, A. G. González, and L. Kondic, *J. Phys. Conf. Ser.* **166**, 012009 (2009).
- [26] M. Wilczek, W. Tewes, S. Engelkemper, S. V. Gurevich, and U. Thiele, *Phys. Rev. Lett.* **119**, 204501 (2017).
- [27] H. M. J. M. Wedershoven, C. W. J. Berendsen, J. C. H. Zeegers, and A. A. Darhuber, *Appl. Phys. Lett.* **104**, 054101 (2014).
- [28] M. L. Rocca, C. Adduce, V. Lombardi, G. Sciortino, and R. Hinkelmann, *Int. J. Numer. Methods Fluids* **70**, 1048 (2012).
- [29] O. Reynolds, *Philos. Trans. R. Soc. Lond.* **174**, 935 (1883).
- [30] A. Sommerfeld, *Int. Congr. Math.* **3**, 116 (1908).
- [31] A. Cali, S. Succi, A. Cancelliere, R. Benzi, and M. Gramignani, *Phys. Rev. A* **45**, 5771 (1992).
- [32] R. D. Kingdon and P. Schofield, *J. Phys. A* **25**, L907 (1992).
- [33] S. Chen, S. Dawson, G. Doolen, D. Janecky, and A. Lawniczak, *Comput. Chem. Eng.* **19**, 617 (1995).
- [34] J. R. Weimar and J. P. Boon, *Physica A (Amsterdam)* **224**, 207 (1996).
- [35] M. R. Swift, E. Orlandini, W. R. Osborn, and J. M. Yeomans, *Phys. Rev. E* **54**, 5041 (1996).
- [36] S. V. Lishchuk, C. M. Care, and I. Halliday, *Phys. Rev. E* **67**, 036701 (2003).

- [37] A. K. Gunstensen, D. H. Rothman, S. Zaleski, and G. Zanetti, *Phys. Rev. A* **43**, 4320 (1991).
- [38] M. Junk and A. Klar, *SIAM J. Sci. Comput.* **22**, 1 (2000).
- [39] S. P. Thampi, S. Ansumali, R. Adhikari, and S. Succi, *J. Comput. Phys.* **234**, 1 (2013).
- [40] L. Rayleigh, *Proc. London Math. Soc.* **s1-14**, 170 (1882).
- [41] G. Taylor, *Proc. R. Soc. Lond. A* **201**, 192 (1950).
- [42] H. Kull, *Phys. Rep.* **206**, 197 (1991).
- [43] D. H. Sharp, *Physica D (Amsterdam)* **12**, 3 (1984).
- [44] P. G. de Gennes, *Rev. Mod. Phys.* **57**, 827 (1985).
- [45] L. H. Tanner, *J. Phys. D* **12**, 1473 (1979).
- [46] J. H. Snoeijer and B. Andreotti, *Annu. Rev. Fluid Mech.* **45**, 269 (2013).
- [47] R. Rioboo, M. Marengo, and C. Tropea, *Exp. Fluids* **33**, 112 (2002).
- [48] E. Jambon-Puillet, O. Carrier, N. Shahidzadeh, D. Brutin, J. Eggers, and D. Bonn, *J. Fluid Mech.* **844**, 817 (2018).
- [49] A. Cazabat and M. C. Stuart, *J. Phys. Chem.* **90**, 5845 (1986).
- [50] J.-D. Chen, *J. Colloid Interface Sci.* **122**, 60 (1988).
- [51] C. Furmidge, *J. Colloid Sci.* **17**, 309 (1962).
- [52] T. Podgorski, J.-M. Flesselles, and L. Limat, *Phys. Rev. Lett.* **87**, 036102 (2001).
- [53] H.-Y. Kim, H. Lee, and B. Kang, *J. Colloids Surf. Sci.* **247**, 372 (2002).
- [54] M. Sbragaglia, L. Biferale, G. Amati, S. Varagnolo, D. Ferraro, G. Mistura, and M. Pierno, *Phys. Rev. E* **89**, 012406 (2014).
- [55] K. Kargupta and A. Sharma, *Langmuir* **18**, 1893 (2002).
- [56] B. J. Brasjen, H. Gu, and A. A. Darhuber, *Microfluid Nanofluid.* **14**, 669 (2013).
- [57] S. Chandrasekaran and G. Juckeland, *OpenACC for Programmers: Concepts and Strategies*, 1st ed. (Addison-Wesley Professional, London, 2017).